Induced polarization of clay-rich materials - Part 1: The effect of desiccation

André Revil, Ahmad Ghorbani, Damien Jougnot, Béatrice Yven

GEOPHYSICS, VOL. 88, NO. 4 (JULY-AUGUST 2023); P. 1–16, 17 FIGS., 7 TABLES.
10.1190/GEO2022-0510.1

Induced polarization of clay-rich materials — Part 1: The effect of desiccation

André Revil[1], Ahmad Ghorbani[2], Damien Jougnot[3], and Béatrice Yven[4]

ABSTRACT

A petrophysical model describing spectral induced polarization (IP) has been developed for clay rocks accounting for the Maxwell-Wagner polarization. It is also used to connect the complex conductivity to the relative permeability of the material. This model is applied to the Callovo-Oxfordian clay rock of the Paris Basin (France) where the Meuse/Haute-Marne Underground Research Laboratory is located. Laboratory experiments are performed using eight clay-rock cores to study the effect of desiccation on their spectral-IP response. The measurements are performed along the foliation plane. Complex conductivity spectra are measured over a frequency range of 1 mHz to 45 kHz. These spectra are fitted with a double Cole-Cole model to extract the evolution of the Cole-Cole parameters with the saturation during the desiccation process. The low-frequency Cole-Cole model corresponds to IP phenomena, whereas the high-frequency Cole-Cole model corresponds to the Maxwell-Wagner contribution. We obtain the value of the first and second Archie's exponents and we check the relationship between the surface conductivity and the cation exchange capacity of the clay rocks. We are also able to connect the relative permeability curve to the second (saturation) Archie's exponent. The monitoring of the complex conductivity can be used to predict how the permeability of the clay-rock formation changes with the water content.

INTRODUCTION

The monitoring of the excavation damaged zone (EDZ) around galleries used for long-term repositories of radioactive wastes is an important task for evaluating their safety (Volckaert et al., 2004). In the Meuse/Haute-Marne Underground Research Laboratory (URL, Paris Basin, France), the French national agency for radioactive waste management (Agence Nationale pour la gestion des Déchets RadioActifs [ANDRA]) has developed an extensive research program to understand the evolution of the EDZ and its properties (Armand et al., 2014). This URL is built in the Callovo-Oxfordian (COx) clay-rock formation of the Paris Basin. This formation is mainly composed of clay minerals (20%–55% of the rock), tectosilicates (25%–35%), calcite (15%–30%), and secondary minerals (less than 5% of the total; Vinsot et al., 2014). The secondary minerals include dolomite, feldspar, hematite, and small proportions of pyrite (see Yven et al., 2007; Vinsot et al., 2014; see Figure 1). Clay minerals consist mostly of a mixture of illite and micas, interstratified illite/smectite, kaoline, and chlorite in various proportions depending on the depth (Yven et al., 2007).

In the past, electrical conductivity tomography has been applied to the EDZ (e.g., Kiewer, 2000; Yaramanci and Kiewer, 2000; Kruschwitz, 2002). Subsequently, preliminary works have been performed to see how induced polarization (IP) can be used to study the EDZ (Kruschwitz and Yaramanci, 2004; Jougnot et al., 2010a, 2010b; Okay et al., 2013). IP can be seen as an extension of the electrical conductivity/resistivity method but accounts for the polarization mechanisms of the porous materials and therefore for the frequency dependence of the electrical conductivity itself (Bleil, 1948, 1953). The term "IP" is mostly related to low-frequency (<10 kHz) polarization phenomena affecting insulating grains coated by their electrical double layer (Jougnot et al., 2010a; Okay et al., 2013). In addition, the presence of semiconductors (e.g., pyrite and magnetite)

Manuscript received by the Editor 12 August 2022; revised manuscript received 26 February 2023; published ahead of production 28 March 2023.
[1]Université Grenoble Alpes, Université Savoie Mont Blanc, CNRS, EDYTEM, Le Bourget du Lac, France. E-mail: andre.revil@univ-smb.fr (corresponding author).
[2]Naga Geophysics, Technolac, Le Bourget du Lac 73370, France. E-mail: ahmad.ghorbani@naga-geophysics.com.
[3]Sorbonne Université, CNRS, EPHE, UMR 7619 METIS, Paris, France. E-mail: damien.jougnot@upmc.fr.
[4]ANDRA, Scientific and Technical Division, Châtenay-Malabry Cedex, France. E-mail: beatrice.yven@andra.fr.

may play a role in the low-frequency complex conductivity response of these rocks (Okay et al., 2013; Revil et al., 2015a, 2015b); however, in the COx formation, the amount of pyrite is low (a few percent at most). Tartrat et al. (2019) show that pyrite influences complex conductivity only at very low water contents. The Cole-Cole parametric model offers a good starting model to fit the complex conductivity spectra (e.g., Dias, 1972, 2000; Flekkøy, 2013).

The research questions tackled in this paper are the following. (1) Can we fit the complex conductivity spectra with a double Cole-Cole model? (2) How do the Cole-Cole parameters evolve with the desiccation of the clay rock? (3) Can we predict or explain the observed trends between the Cole-Cole parameters and saturation to the light of a physics-based model? (4) Can we predict the evolution of the relative permeability of the formation from the parameters derived from the complex conductivity spectra?

To respond to these fundamental questions, we first develop a descriptive parametric model for the complex conductivity of clay rocks. Then, we present experimental data showing complex conductivity spectra obtained in a broad saturation range using eight core samples of the COx formation. These spectra are inverted in terms of a double Cole-Cole model, and then the dependence of the Cole-Cole parameters with the saturation and the cation exchange capacity (CEC) are analyzed and discussed. Finally, we focus on the COx formation relative permeability curve to demonstrate that this curve can be predicted from the saturation exponent derived from the complex conductivity spectra.

THEORY

A combined polarization model

We consider an isotropic, homogeneous, and linear elementary representative volume of a porous material. The total current density $\mathbf{J}$ (A m^{-2}) that is defined through Ampère's law (actually the form of Ampère's law derived by James Clerk Maxwell including the displacement current) is given by

$$\nabla \times \mathbf{H} = \mathbf{J}, \tag{1}$$

where $\mathbf{H}$ denotes the auxiliary magnetic field (A m^{-1}) and the total current density $\mathbf{J}$ is the sum of a conduction current, a diffusion current (the driving force for the movement of the ionic charge carriers is an electrochemical potential; see Jamnik and Maier, 2001; Revil, 2013), and a displacement current density. The conduction and diffusion current densities can be combined in an equivalent Ohm's law with a complex conductivity (e.g., Leroy et al., 2008). This yields

$$\mathbf{J} = \sigma^* \mathbf{E} + \frac{\partial \mathbf{D}}{\partial t}. \tag{2}$$

The electric displacement field $\mathbf{D}$ (electric induction, in C m^{-2}) is related to the electrical field $\mathbf{E}$ by $\mathbf{D} = \varepsilon^* \mathbf{E}$, where ε^* denotes the dielectric constant or permittivity (F m^{-1}) of the material including the Maxwell-Wagner polarization effect as discussed next. The expression of the effective conductivity $\hat{\sigma}*$ (or the effective complex permittivity $\hat{\varepsilon}*$) of the porous material entering Ampère's law is

$$\nabla \times \mathbf{H} = \hat{\sigma}^* \mathbf{E} (= i\omega \hat{\varepsilon}^* \mathbf{E}), \tag{3}$$

where i denotes the pure imaginary number ($i^2 = -1$) and we assume that all the fields are harmonic $\mathbf{E} = \mathbf{E}_0 \exp(i\omega t)$.

We assume K-dielectric polarization mechanisms and N-IP mechanisms. The Cole-Cole model is a parametric function initially used to describe dielectric phenomena (Cole and Cole, 1941). It assumes that the distribution of the microheterogeneities responsible for the distribution of the relaxation times is approximately a log-normal distribution. Assuming that each polarization mechanism can be approximated by a Cole-Cole function, the expression of the effective complex permittivity is given by

$$\hat{\varepsilon}^* = -i \frac{\hat{\sigma}^*}{\omega}, \tag{4}$$

$$\hat{\varepsilon}^* = \varepsilon_\infty + \sum_{k=1}^{K} \frac{\varepsilon_k^0 - \varepsilon_k^\infty}{1 + (i\omega\tau_k)^{c_k}} - \frac{i}{\omega} \left(\sigma_\infty - \sum_{n=1}^{N} \frac{\sigma_n^\infty - \sigma_n^0}{1 + (i\omega\tau_n)^{c_n}} \right), \tag{5}$$

where the high-frequency conductivity and low-frequency dielectric constant are given by

$$\sigma_\infty = \sum_{n=1}^{N} \sigma_n^\infty, \tag{6}$$

$$\sigma_0 = \sum_{n=1}^{N} \sigma_n^0, \tag{7}$$

$$\varepsilon_\infty = \sum_{k=1}^{K} \varepsilon_k^\infty, \tag{8}$$

$$\varepsilon_0 = \sum_{k=1}^{K} \varepsilon_k^0, \tag{9}$$

where τ_k (s) denotes a relaxation time for the dielectric polarization process k (including alpha and delta polarization phenomena corresponding to the IP and Maxwell-Wagner polarization phenomena, respectively); ε_k^0 and ε_k^∞ denote the low- and high-frequency dielectric constants for the polarization process labeled k, respectively ($\Delta\varepsilon_k = \varepsilon_k^0 - \varepsilon_k^\infty$ is called the dielectric increment); and $0 \leq c_k \leq 1$ denotes the Cole-Cole exponent for dielectric polarization process k. The last term in equation 5 corresponds to α-polarization phenomena and can be associated for instance with different grain-size distributions modeled by log-normal distributions (e.g., fine and coarse grains) and the presence of semiconductors (pyrite and magnetite). In this contribution, σ_0 denotes the direct current (DC) conductivity; σ_n^0 and σ_n^∞ denote the low- and high-frequency conductivities associated with contribution n, respectively ($M_n^j = \sigma_j^\infty - \sigma_j^0$ is called the partially normalized chargeability of contribution j); τ_n denotes the relaxation time for the α-contribution n; and $0 \leq c_n \leq 1$ denotes the Cole-Cole exponent n. Equation 5 works if we have polarization processes working in different frequency ranges, which is generally the case as discussed next with specific examples.

In porous media, the mechanisms of polarization in the frequency range of 1 mHz to 10 GHz are limited to the mechanisms of the IP associated with the polarization of the electrical double-layer-coating insulating grains and the polarization of the metallic particles. In addition, we have two other mechanisms of dielectric polarization called the Maxwell-Wagner polarization and the polarization of the sorbed water and the free water molecules at high frequencies (GHz range; see Grosse, 2002). If we are dealing with two (i.e., $K = 2$) dielectric polarization mechanisms, namely, the Maxwell-Wagner polarization and the polarization of the water molecules (gamma polarization, see Appendix A), and two mechanisms of IP (i.e., $N = 2$), namely, the polarization of pyrite and the polarization of the clay minerals, we have the following formula:

$$\hat{\varepsilon}^* = \varepsilon_\infty + \frac{\varepsilon^0_{\mathrm{MW}} - \varepsilon^\infty_{\mathrm{MW}}}{1 + (i\omega\tau_{\mathrm{MW}})^{c_{\mathrm{MW}}}} + \frac{\varepsilon^0_W - \varepsilon^\infty_W}{1 + i\omega\tau_w} - \frac{i\sigma_\infty}{\omega}\left(1 - \sum_{k=1}^{K}\frac{M_k}{1 + (i\omega\tau_k)^{c_k}}\right), \quad (10)$$

$$M_k = \frac{\sigma^\infty_k - \sigma^0_k}{\sigma_\infty}, \quad (11)$$

$$\sigma_0 = \sigma_\infty\left(1 - \sum_{k=1}^{K} M_k\right), \quad (12)$$

$$\tau_{\mathrm{MW}} = \frac{\varepsilon_S + 2\varepsilon_w}{\sigma_S + 2\sigma_w}, \quad (13)$$

where c_{MW} denotes the Cole-Cole exponent for the Maxwell-Wagner relaxation process; M_k, σ^∞_k, σ^0_k, and c_k denote the chargeability, instantaneous conductivity, DC conductivity, and Cole-Cole exponent associated with the IP process k, respectively; and σ_∞ denotes the total instantaneous conductivity of the material for the combined effects of the IP mechanisms.

In equation 13, the quantities ε_S and ε_w are the dielectric constants for the solid and water phases, respectively ($\varepsilon_S \ll 2\varepsilon_w$), and σ_S (surface conductivity) and σ_w are the grain and pore water conductivity, respectively. The expression of the relaxation time in equation 13 for the Maxwell-Wagner polarization is from Grosse (2002). At low salinities, it can be approximated by $\tau_{\mathrm{MW}} = 2\varepsilon_w/\sigma_S = 160 \times 8.854 \times 10^{-12}$ C/Vm/3×10^{-2} S/m $\approx 5 \times 10^{-8}$ s. When the pore water conductivity dominates the surface conductivity, the relaxation time is given by the well-known formula $\tau_{\mathrm{MW}} = \varepsilon_w/\sigma_w$. For a pore water conductivity of 10^{-3} S/m, we have $\tau_{\mathrm{MW}} = \varepsilon_w/\sigma_w = 80 \times 8.854 \times 10^{-12}$C/Vm/$10^{-3}$S/m $= 7 \times 10^{-7}$s. Note that at higher salinities, this relaxation time would be even smaller. Therefore, the Maxwell-Wagner polarization is occurring at very high frequencies quite above the frequency range investigated in this paper (<45 kHz) but it may overlap with the IP of the clay grains, which is the main contributor in the investigated frequency range. The role of the Maxwell-Wagner polarization in clay-rich materials is underlined by Cosenza et al. (2008).

Simplified model

We are interested now in IP phenomena below a frequency of 45 kHz and therefore the polarization of the water molecules can be safely neglected. We consider two IP processes and we write an expression for the effective conductivity of the clay rock as

$$\hat{\sigma}^* \asymp \sigma_\infty\left(1 - \frac{M_1}{1 + (i\omega\tau_1)^{c_1}} - \frac{M_2}{1 + (i\omega\tau_2)^{c_2}}\right), \quad (14)$$

$$\sigma_\infty = \sigma^\infty_1 + \sigma^\infty_2, \quad (15)$$

$$\sigma_0 = \sigma_\infty(1 - M_1 - M_2), \quad (16)$$

where M_1 and M_2 are the chargeabilities (dimensionless), c_1 and c_2 are the two Cole-Cole exponents (dimensionless), and τ_1 and τ_2 are the (relaxation) time constants (expressed in s). Indices 1 and 2 refer to two dispersion processes, respectively. If the total chargeability is defined by $M = (\sigma_\infty - \sigma_0)/\sigma_\infty$, we have $M = M_1 + M_2$.

In our model, one of the two mechanisms of polarization (e.g., mechanism 1) corresponds to the polarization of the electrical double layer associated with the insulating grains, whereas the second mechanism (mechanism 2) corresponds to the Maxwell-Wagner polarization. The first (low-frequency) polarization mechanism is discussed and described in the next section.

Matrix contribution to IP

Using a volume-averaging approach, Revil (2013) obtains two expressions for the high- and low-frequency conductivities of a clay-rich material. The current situation is further complicated by the fact that the clay rock is considered to be partially saturated by desiccation. In this case, the salt remains segregated in the liquid pore water and salinity increases with the decrease of the saturation during desiccation. The conductivity of the pore water $\sigma_w(s_w)$ scales therefore as σ_w/s_w (σ_w denotes the conductivity of the pore water when the sample is fully saturated, which is the initial pore water conductivity in the drying experiment). Accounting for this effect, the model of Revil (2013, their equations 61 and 62) is modified and leads to the following expressions for the instantaneous conductivity and DC conductivity of the COx formation: respectively,

$$\sigma^\infty_1 = s_w^{n-1}\left[\frac{1}{F}\sigma_w + \left(\frac{1}{F\phi}\right)\rho_g B\mathrm{CEC}\right], \quad (17)$$

$$\sigma^0_1 = s_w^{n-1}\left[\frac{1}{F}\sigma_w + \left(\frac{1}{F\phi}\right)\rho_g (B - \lambda)\mathrm{CEC}\right], \quad (18)$$

where $n > 1$ (dimensionless) denotes the saturation exponent (also called the second Archie's exponent), s_w (dimensionless) denotes the liquid pore water saturation, σ_w (S m^{-1}) denotes the initial pore water conductivity at full saturation, F (dimensionless) denotes the intrinsic formation factor related to the connected porosity ϕ

(dimensionless) by the first Archie's law $F = \phi^{-m}$ where $m > 1$ (dimensionless) is called the porosity or first Archie's exponent (Archie, 1942), ρ_g is the grain density (usually $\rho_g = 2650$ kg m^{-3}), and CEC denotes the cation exchange capacity (C kg^{-1} or meq/100 g with 1 meq/100 g = 963.20 C kg^{-1}). The quantity B (expressed in m^2 s^{-1} V^{-1}) denotes the apparent mobility of the counterions for surface conduction and λ (expressed in m^{2}s^{-1} V^{-1}) denotes the apparent mobility of the counterions for the polarization associated with the quadrature conductivity (see Revil et al., 2017a, 2017b). A dimensionless number R is also introduced by $R = \lambda/B$ (see Revil et al., 2017a, 2017b, 2017c). From Ghorbani et al. (2018), we have $\beta(Na^+, 25°C) = 3.1 \pm 0.3 \times 10^{-9}$ m^{-2} s^{-1} V^{-1} and $\lambda(Na^+, 25°C) = 3.0 \pm 0.7 \times 10^{-10}$ m^{-2} s^{-1} V^{-1} and R is typically approximately 0.09 $\pm$ 0.01 (independent of the temperature and saturation). This dimensionless number also is the ratio of the normalized chargeability to the surface conductivity. Note that the dependence of the surface conductivity and normalized chargeability (or quadrature conductivity) with saturation are consistent with the model and data sets discussed in Waxman and Smits (1968) and Vinegar and Waxman (1984).

From equations 11, 17, and 18, we obtain the following expression of the chargeability of the COx formation (neglecting the effect of pyrite):

$$M_1 = \frac{\rho_g \lambda \mathrm{CEC}}{\phi \sigma_w + \rho_g B \mathrm{CEC}} \leq R \equiv \frac{\lambda}{B}. \tag{19}$$

This equation shows explicitly the dependence among the background chargeability M_1, the pore water conductivity, and the CEC. Therefore, the background chargeability is generally quite small (less than 10% or 100 mV/V).

The Cole-Cole time constant τ_1 is associated with characteristic pore size Λ according to (Revil and Florsch, 2010; Revil et al., 2012)

$$\tau_1 = \frac{s_w^2 \Lambda^2}{2 D_{(+)}^S}, \tag{20}$$

where $D_{(+)}^S$ (m^2 s^{-1}) denotes the diffusion coefficient of the counterions in the Stern layer. The value of this diffusion coefficient is $D_{(+)}^S = 3.8 \times 10^{-12}$ m^2 s^{-1}. In terms of access size from mercury porosimetry, we have measured $r_c = 20$ nm. This size is related to pore size Λ by $r_c = 5.3\ \Lambda$ (Revil et al., 2014). Therefore, it yields $\Lambda = 4$ nm. Here, $\tau_1 = 2 \times 10^{-6}$ s, which is comparable to the relaxation time associated with the Maxwell-Wagner polarization. In other words, it would be difficult to say if the mechanism labeled 2 in equation 14 is related to the polarization of the clay minerals or the Maxwell-Wagner polarization.

Another lower frequency mechanism can be associated with the large grains present in the COx formation (see Figure 1). For the large grains, the associated relaxation time is given by (Revil et al., 2021)

$$\tau_1 = \frac{d^2 s_w^2 \phi^2}{16 D_{(+)}^S}. \tag{21}$$

Using $D_{(+)}^S = 2.5 \times 10^{-9}$ m^2 s^{-1}, $\phi = 0.20$, $d = 90$ µm yields $\tau_2 \approx 10^{-2}$ s. Thus, the large grains are responsible for a low-frequency polarization mechanism that can be fully observed in the frequency range investigated in our study. An increase in the relaxation time with saturation also is observed in Binley et al. (2005).

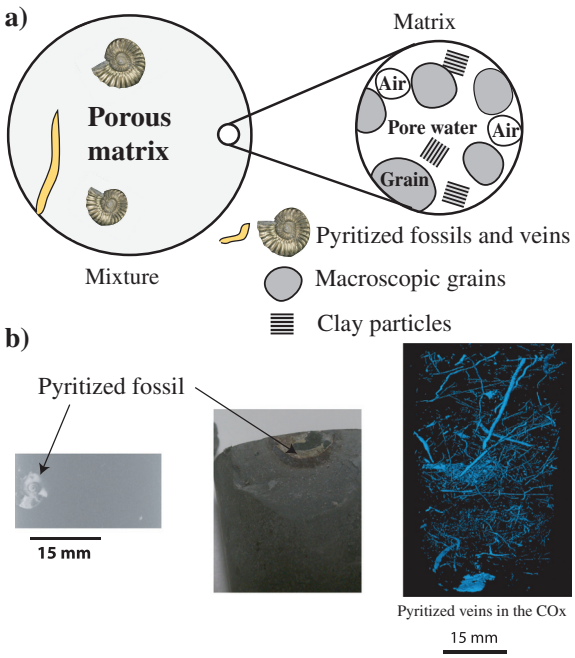

Figure 1. Clay rock considered as a composite of a partially saturated background plus pyrite grains. (a) The polarization is coming from the clay particles plus an effect of the pyrite grains. We want to study the IP signature of this composite undergoing desiccation. (b) X-ray tomography reveals that pyrite is usually associated with fossils and vugs corresponding to bioturbation.

Connection to permeability

We discuss now the connection between the permeability and the electrical properties described previously. The permeability k (m^2) at a given water saturation s_w is given by the product of the permeability at saturation and relative permeability k_r (dimensionless):

$$k(s_w) = k_r(s_w) k_S. \tag{22}$$

The permeability at saturation k_S is typically related to porosity and pore size. In the present case, we use a clay content estimate based on the CEC. We follow Sen et al. (1990) in obtaining the permeability at saturation from the CEC (C kg^{-1}) and the formation factor F according to

$$k_S = k_0 \left(\frac{1}{F Q_V} \right)^c, \tag{23}$$

where k_0 and c are the two fitting parameters, $F = \phi^{-m}$, and $Q_V = \rho_g (1 - \phi)\mathrm{CEC}/\phi$ with $\rho_g = 2650$ kg m^{-3} (grain density of the solid phase composed of silicates). For instance, for volcanic rocks from the White islands (New Zealand), Revil et al. (2020) obtain $k_0 = 1.46 \times 10^6$ and $c = 2.88$. Using these parameters with $F = 30$ and $Q_V = 300 \times 10^6$ C m^{-3} (using $\phi = 0.15$ and CEC = 20 meq/100 g), we obtain a permeability for the COx of

0.6×10^{-20} m^2, which is the correct order of magnitude for the permeability of the COx (see the companion paper Revil et al., forthcoming). The quantity Q_V denotes the total excess of charge per unit pore volume (C m^{-3}). The relative permeability is given by (see Revil, 2013)

$$k_r(s_w) = \left(\frac{s_w - s_w^i}{1 - s_w^i}\right)^{n+2}, \tag{24}$$

where s_w^i (dimensionless) is the irreducible water saturation. We test equation 24 in the next section. The saturation exponent n and the value of the irreducible water saturation s_w^i are independently obtained from the complex conductivity data.

MATERIALS AND METHODS

We use eight core samples: three core samples (EST59676, EST59674, and EST59620) from the COx formation and five core samples from the study by Jougnot et al. (2010a) (samples EST27906, EST28144, EST29296, EST29300, and EST30749). The properties of the core samples are presented in Table 1. The CEC and specific surface area Ssp (based on the Brunauer–Emmett–Teller, BET), theory of the COx are correlated and compared with the literature data for clay minerals and soils in Figure 2. The samples are put in a desiccation chamber and the complex conductivity spectra are obtained with a ZEL-SIP04-V02 impedance meter working in the frequency range of 1 mHz to 45 kHz (Figure 3). The formation factors and surface conductivity data are obtained by plotting the in-phase conductivity data at 1 Hz versus the pore water conductivity and fitting a linear conductivity model from which the formation factor and the surface conductivity can be determined using analysis in a log-log scale (for a recent analysis and a complete description of the methodology, see Revil et al., 2022).

The samples contain the in situ pore water solution and were not resaturated with synthetic pore water. Due to transport issues, the core samples were not fully saturated ($s_w < 0.80$) and were estimated afterward using the procedure described by Jougnot et al. (2010a). Complex conductivity measurements were performed at different water saturations using changes in the relative humidity of the desiccation chamber. Figure 4 shows the desiccation-saturation procedure for a given core sample. For the lower saturation, we use the approach proposed by Cosenza et al. (2007). The samples were prepared in an oven (for 24 h at 70°C, 90°C, and 105°C) and brought back at ambient temperature before performing the measurements.

Table 1. Petrophysical parameters for the eight core samples.

Sample	Depth (m)	ϕ	CEC (meq/100 g)	BET *S*sp (m^2/g)
EST27906	518.16	0.157	24.7	25
EST28144	582.16	0.176	42.4	48
EST29296	617.52	0.163	41.9	53
EST29300	624.38	0.146	43.2	50
EST30749	608.07	0.181	42.5	48
EST59676	490.00	0.203	16.8	30
EST59674	490.00	0.229	16.9	30
EST59620	490.00	0.253	21.8	29

There are three core samples, EST59676, EST59674, and EST59620 from the COx formation, and five core samples from the study of Jougnot et al. (2010a; samples EST27906, EST28144, EST29296, EST29300, and EST30749). The new samples also belong to different facies with respect to the former samples. Samples EST59676, EST59674, and EST59620 are from horizontal wells drilled in the underground laboratory. BET *S*sp denotes the specific surface area of the core samples.

RESULTS AND INTERPRETATION

Complex conductivity spectra

In Figures 5, 6, and 7, we show the complex conductivity spectra at different water saturations. The plain lines correspond to the fit of the data with the double Cole-Cole model discussed in Appendix B. First, we note that this complex conductivity parametric model fits the data very well at nearly all the saturations. The values of the Cole-Cole parameters are provided in Tables 2, 3, 4, 5, and 6. The relaxation times τ_1 and τ_2 are typically approximately 10^{-1} and 10^{-6} s, respectively. This implies that the highest relaxation times (low-frequency polarization) could be associated with the coarser grains, whereas the lowest relaxation time could be associated with the clay grains and the Maxwell-Wagner polarization.

Cole-Cole parameters versus saturation

In Figure 8, we plot the instantaneous conductivity of the rock sample as a function of the saturation. We fit the data using $\sigma_\infty = s_w^{n-1}\sigma_\infty(s_w = 1)$ (from equation 17). This power-law relationship provides the value of the instantaneous conductivity of

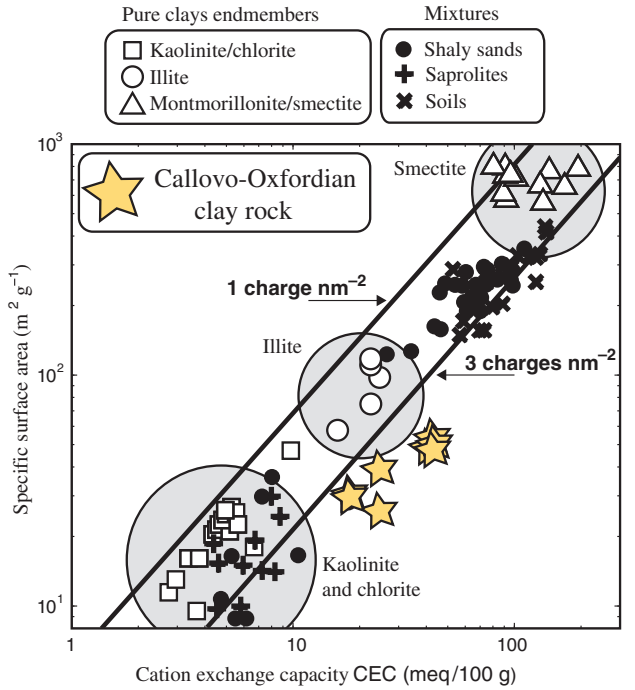

Figure 2. Specific surface area versus CEC (expressed in meq g^{-1} with 1 meq g^{-1} = 96,320 C kg^{-1}). The two lines correspond to a surface charge density of 1–3 elementary charges per unit surface area. The figure shows a comparison between the data for pure clays, soils, and core samples from the COx formation. The trend corresponds to a surface charge density of 4–5 elementary charges per nm^2.

the rock at saturation $\sigma_\infty(s_w = 1)$ and the saturation exponent n. We observe that the value of n is constant over three distinct saturation ranges and that the trend of the conductivity is different above and below a critical saturation value of $s_w^i = 0.36$. This value will be considered to be the irreducible water saturation hereinafter. From near saturation to this critical saturation, the value of the saturation exponent is $n = 2.6 \pm 0.1$. Below the critical saturation of 0.20, for which further desaturation is obtained by heating, the saturation exponent is close to $n = 4.7 \pm 0.9$ probably because of the formation of microcracks and an increase in the local heterogeneity of the core sample (see also the discussion in Ghorbani et al., 2009). For the intermediate saturation range (between 0.20 and 0.36), the conductivity versus saturation conforms also to a second Archie's law with a saturation exponent of $n = 4.1 \pm 0.1$.

In Figure 9, we plot the two Cole-Cole exponents versus the pore water saturation. The low-frequency Cole-Cole exponent c_1 (Figure 9a) also exhibits three domains in the saturation range investigated in this study. Again, we see clearly the two critical saturations discussed previously (0.20 and 0.36). Above the residual water saturation of 0.36, the low-frequency Cole-Cole exponent

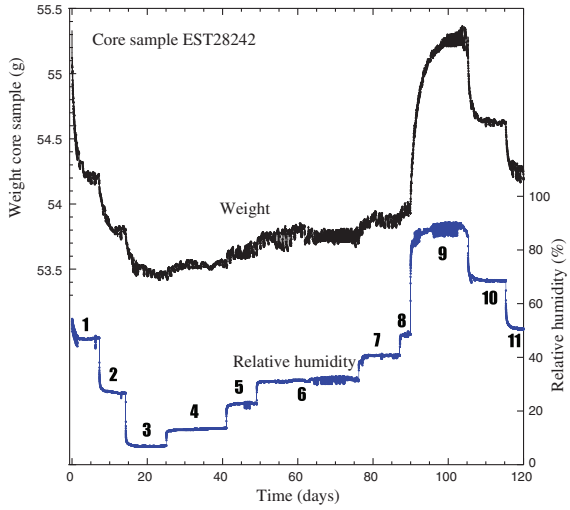

Figure 4. Evolution of the weight of the core sample over time for 11 changes in the relative humidity of the desiccation chamber. The data set shows an example of a desiccation/rehydration cycle.

Figure 3. Impedance meter and electrodes used for the complex conductivity spectra. (a) Setup showing the carbon film electrodes with hydrogel for injection (A and B) and the Ag-AgCl nonpolarizable electrode for potential (M and N). (b) ZEL-SIP04-V02 impedance meter (Zimmermann et al., 2007, 2008) working in the frequency range of 1 mHz to 45 kHz. (c) Detail of the automated humidity system of the environmental chamber (modified from Likos and Lu, 2003).

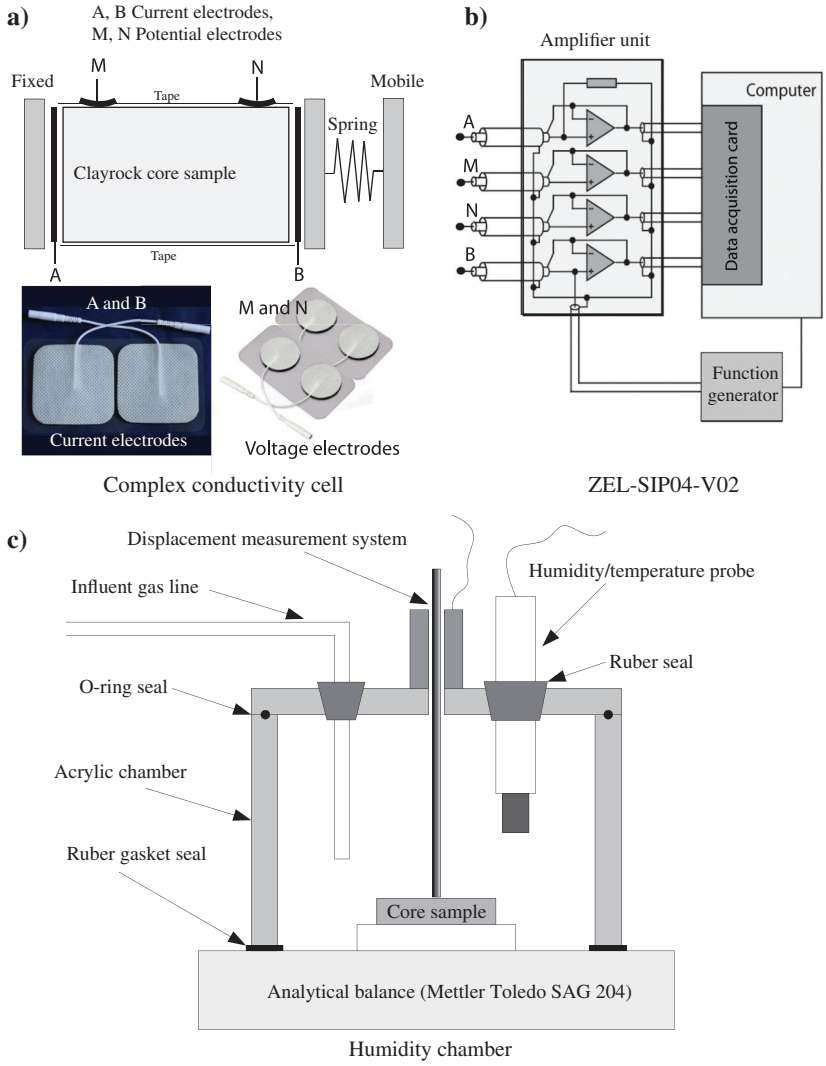

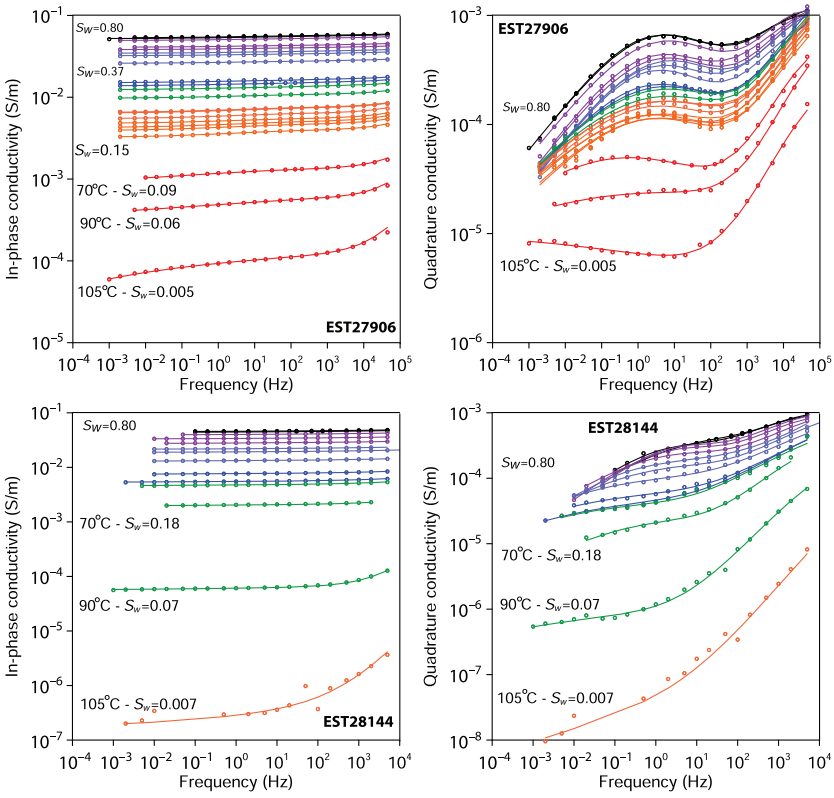

Figure 5. Complex conductivity spectra of core samples EST27906 and EST28144. The plain lines correspond to the fit with a double Cole-Cole model described in Appendix A. The very states below 20% saturation are obtained by heating the core samples, which is likely responsible for mechanical damage through the formation of microcracks.

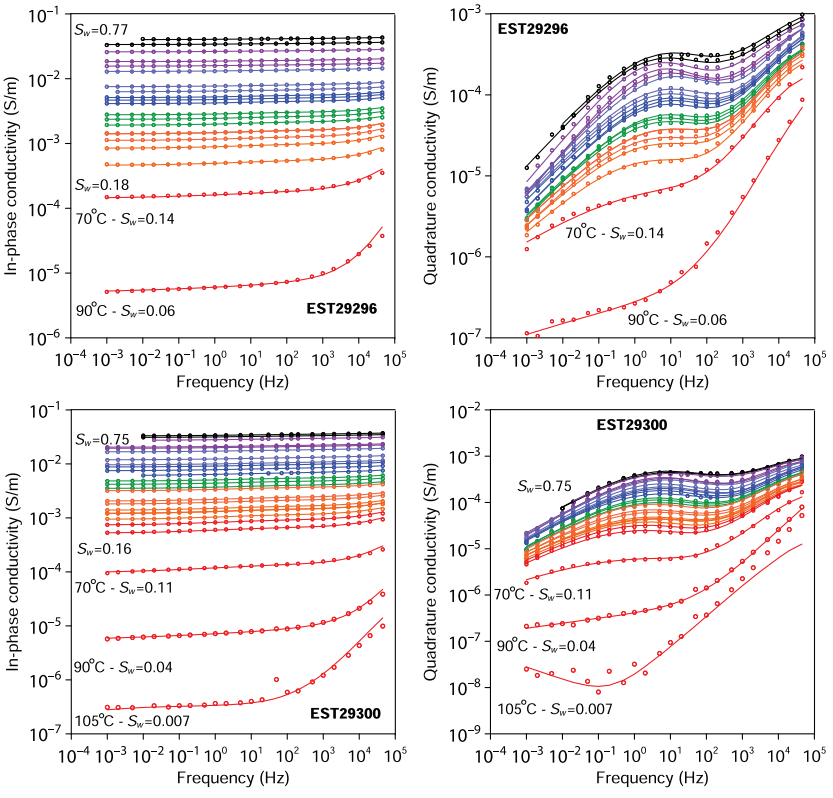

Figure 6. Complex conductivity spectra of core samples EST29296 and EST29300. The plain lines correspond to the fit with a double Cole-Cole model. Similar to Figure 3, we can observe a low-frequency polarization peak. The double Cole-Cole model is a very good model that is able to represent the complex conductivity of the COx formation very well.

c_1 is 0.48 (close to the value of 0.50 corresponding to a Warburg function). This could mean that the grain-size distribution associated with the coarse grains is very narrow. Below the critical water saturation of 0.20, the Cole-Cole exponent decreases with the saturation indicating that the broadness of heterogeneities associated with IP is increasing. A possible explanation is that when the core samples are highly saturated ($s_w > 0.36$), the polarization is mostly associated with the coarse grains, which have a relatively narrow grain-size distribution. For lower saturations, the water remains essentially in the small pores and the polarization is dominated by the clays. The grain- and pore-size distributions are broader for the clayey fraction of the material.

Regarding the second Cole-Cole exponent c_2 (Figure 9b), we see a smooth and slight increase in the value of this Cole-Cole exponent with the desiccation process with a mean value around $c_2 = 0.50$ (the Warburg model). It is difficult to explain this trend in terms of underlying physics except if we consider that it is associated with the polarization of the clay grains.

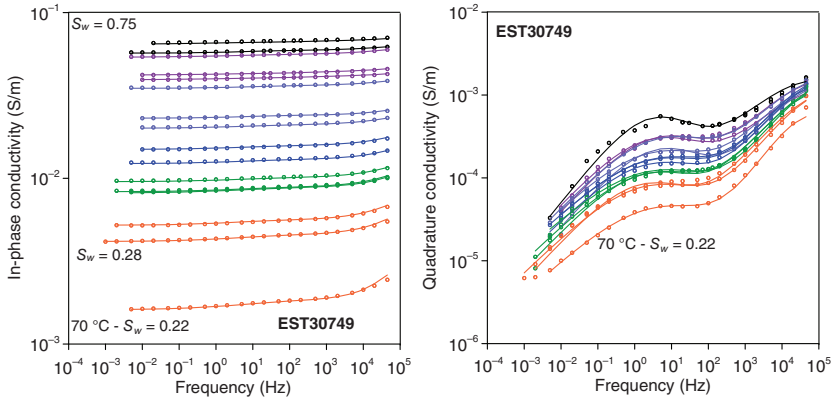

Figure 7. Complex conductivity spectra of sample EST30749. The plain lines correspond to the fit with a double Cole-Cole model. Again we can observe a clear polarization peak at low frequencies. Its position seems independent of saturation.

Table 2. Inversion of the Cole-Cole parameters for the core sample EST27906.

s_w	τ_1 (s)	τ_2 (s)	c_1	c_2	M_1	M_2	σ_∞ (S/m)	rms (%)
0.8	0.035	3.00e-06	0.43	0.48	0.059	0.08	0.061	0.31
0.76	0.047	7.40e-07	0.44	0.39	0.051	0.12	0.064	0.24
0.64	0.029	3.00e-06	0.42	0.55	0.057	0.08	0.057	0.43
0.56	0.043	6.20e-07	0.45	0.42	0.043	0.14	0.05	0.28
0.52	0.032	1.30e-06	0.43	0.51	0.048	0.12	0.046	0.44
0.46	0.026	1.40e-06	0.43	0.53	0.05	0.11	0.041	0.45
0.42	0.042	5.40e-07	0.45	0.46	0.043	0.16	0.041	0.36
0.39	0.05	1.20e-06	0.45	0.49	0.05	0.14	0.032	0.36
0.37	0.048	1.10e-06	0.45	0.51	0.052	0.14	0.03	0.39
0.28	0.05	4.70e-07	0.39	0.52	0.064	0.24	0.022	0.4
0.26	0.038	2.60e-07	0.37	0.56	0.063	0.34	0.023	0.26
0.25	0.034	6.10e-07	0.35	0.58	0.078	0.26	0.019	0.3
0.22	0.034	6.80e-07	0.34	0.61	0.082	0.31	0.016	0.34
0.21	0.051	4.60e-07	0.34	0.6	0.079	0.45	0.01	0.73
0.2	0.041	6.10e-07	0.34	0.6	0.098	0.36	0.012	0.41
0.19	0.04	3.00e-07	0.33	0.57	0.088	0.44	0.013	0.37
0.18	0.051	5.90e-07	0.35	0.62	0.089	0.44	0.012	0.52
0.17	0.059	4.30e-07	0.35	0.58	0.078	0.45	0.01	0.75
0.17	0.045	6.70e-07	0.32	0.62	0.11	0.42	0.0089	0.6
0.16	0.069	3.00e-07	0.35	0.57	0.094	0.48	0.0091	0.67
0.15	0.057	4.60e-07	0.35	0.6	0.096	0.5	0.0081	0.92
0.09	0.31	1.00e-06	0.27	0.65	0.15	0.55	0.0031	0.34
0.06	0.068	8.90e-07	0.17	0.72	0.17	0.67	0.002	0.41
0.005	—	7.40e-07	0.095	0.66	0.31	0.81	0.00079	0.55

Figure 10 shows the low-frequency normalized chargeability $M_n^1 = \sigma_1^\infty - \sigma_1^0$ (Figure 10a) and the high-frequency chargeability (Figure 10b) of the clay rock versus saturation. The low-frequency normalized chargeability exhibits the same trends as the instantaneous conductivity (Figure 8). This behavior is expected from the model and we recover more or less the same values of the saturation exponents as expected from equations 17 and 18. In Figure 10b, we plot the chargeability associated with the high-frequency polarization process versus the saturation. We observe a smooth increase in the chargeability with the desiccation process. Here again, this trend remains difficult to explain with respect to the underlying physics of the polarization processes.

Table 3. Inversion of the Cole-Cole parameters for the core sample EST28144.

s_w	τ_1 (s)	τ_2 (s)	c_1	c_2	M_1	M_2	σ_∞ (S/m)	rms (%)
0.8	0.0097	1.20e-05	0.39	0.52	0.035	0.082	0.051	0.28
0.79	0.058	9.90e-06	0.49	0.41	0.02	0.11	0.051	0.51
0.78	0.043	6.60e-06	0.52	0.43	0.022	0.12	0.046	0.41
0.61	0.04	1.00e-05	0.47	0.48	0.03	0.11	0.039	0.35
0.52	0.051	3.20e-06	0.4	0.45	0.034	0.15	0.034	0.25
0.45	0.07	4.80e-07	0.42	0.44	0.029	0.29	0.031	0.85
0.4	0.071	1.50e-06	0.36	0.43	0.032	0.21	0.025	0.51
0.35	0.23	6.70e-07	0.3	0.38	0.032	0.28	0.019	0.51
0.32	0.098	8.20e-07	0.25	0.43	0.038	0.31	0.014	0.6
0.29	0.39	6.40e-07	0.26	0.41	0.035	0.35	0.012	0.62
0.27	0.45	5.10e-07	0.26	0.42	0.031	0.45	0.01	0.61
0.26	0.81	1.70e-06	0.27	0.43	0.036	0.37	0.0078	0.86
0.18	0.1	9.20e-06	0.33	0.59	0.043	0.34	0.0032	0.71
0.07	0.17	4.10e-06	0.18	0.66	0.022	0.87	0.00049	1

Table 4. Inversion of the Cole-Cole parameters for the core sample EST29296.

s_w	τ_1 (s)	τ_2 (s)	c_1	c_2	M_1	M_2	σ_∞ (S/m)	rms (%)
0.77	0.02231	4.10e-07	0.47268	0.43078	0.03082	0.13497	0.048086	0.55121
0.74	0.0289	3.02e-07	0.49075	0.41848	0.030138	0.15394	0.041307	0.53843
0.6	0.0317	6.85e-07	0.53267	0.45444	0.032415	0.1448	0.031602	0.9117
0.5	0.0267	4.32e-07	0.54529	0.4716	0.03589	0.18545	0.023628	0.69151
0.42	0.02122	3.21e-07	0.51112	0.4939	0.038545	0.2195	0.0211	0.4394
0.38	0.01426	8.13e-07	0.47689	0.59797	0.048274	0.18935	0.016994	0.4233
0.38	0.0153	7.92e-07	0.46835	0.6073	0.051201	0.21937	0.014013	0.39853
0.32	0.02036	4.46e-07	0.466	0.54768	0.050326	0.29122	0.011454	0.42308
0.29	0.02208	7.75e-07	0.46598	0.581	0.053838	0.28047	0.009458	0.37418
0.28	0.02133	5.45e-07	0.45427	0.56043	0.054212	0.33649	0.008406	0.45689
0.27	0.0193	9.83e-07	0.46599	0.59598	0.056847	0.30776	0.007341	0.4709
0.26	0.0227	1.17e-06	0.46343	0.59535	0.058298	0.30421	0.006478	0.56835
0.24	0.02653	1.44e-06	0.4703	0.58386	0.059078	0.33732	0.004601	0.57318
0.22	0.03142	8.90e-07	0.45887	0.57612	0.05751	0.41006	0.004442	0.51518
0.21	0.02628	1.24e-06	0.44061	0.61357	0.06604	0.41066	0.003672	0.65674
0.2	0.03233	1.59e-06	0.4395	0.6163	0.068048	0.42772	0.002822	0.67724
0.2	0.02385	1.48e-06	0.42172	0.63747	0.069186	0.45175	0.002945	0.55203
0.19	0.03782	1.12e-06	0.43634	0.59826	0.057344	0.52393	0.002665	0.55173
0.19	0.03433	1.53e-06	0.41177	0.62748	0.066616	0.52432	0.002067	0.60055
0.18	0.05491	1.39e-06	0.39793	0.62039	0.056479	0.64762	0.001558	0.65789

Table 5. Inversion of the Cole-Cole parameters for the core sample EST29300.

s_w	τ_1 (s)	τ_2 (s)	c_1	c_2	M_1	M_2	σ_∞ (S/m)	rms (%)
0.75	0.026	7.60e-07	0.45	0.43	0.057	0.14	0.041133	0.51
0.74	0.024	7.10e-07	0.44	0.42	0.058	0.14	0.038632	0.42
0.69	0.023	7.00e-07	0.42	0.45	0.066	0.15	0.034844	0.43
0.55	0.031	1.20e-06	0.47	0.5	0.064	0.15	0.026195	0.63
0.52	0.024	1.10e-06	0.44	0.53	0.07	0.15	0.025091	0.43
0.47	0.026	6.90e-07	0.45	0.51	0.071	0.19	0.02257	0.39
0.41	0.033	1.00e-06	0.46	0.52	0.078	0.2	0.016494	0.5
0.37	0.03	1.10e-06	0.44	0.56	0.085	0.21	0.013567	0.53
0.34	0.03	6.90e-07	0.44	0.53	0.082	0.25	0.013117	0.51
0.31	0.034	9.10e-07	0.44	0.55	0.086	0.25	0.01125	0.54
0.3	0.032	9.90e-07	0.4	0.56	0.096	0.26	0.00943	0.3
0.27	0.046	9.30e-07	0.44	0.53	0.084	0.3	0.007783	0.7
0.26	0.046	1.20e-06	0.43	0.55	0.09	0.3	0.006851	0.62
0.25	0.046	1.20e-06	0.42	0.55	0.092	0.32	0.005993	0.61
0.24	0.059	6.90e-07	0.43	0.52	0.082	0.39	0.005987	0.65
0.21	0.067	7.70e-07	0.42	0.52	0.091	0.42	0.004188	0.65
0.2	0.054	1.30e-06	0.4	0.59	0.1	0.4	0.003604	0.65
0.19	0.066	1.50e-06	0.39	0.59	0.099	0.42	0.002908	0.68
0.19	0.055	2.20e-06	0.37	0.62	0.11	0.41	0.00251	0.75
0.18	0.057	2.20e-06	0.38	0.64	0.11	0.41	0.002515	0.75
0.17	0.088	2.00e-06	0.4	0.6	0.11	0.46	0.002149	0.72
0.17	0.095	1.60e-06	0.39	0.6	0.1	0.52	0.00193	0.64
0.16	0.11	1.40e-06	0.38	0.6	0.092	0.6	0.001673	0.66

Table 6. Inversion of the Cole-Cole parameters for the core sample EST30749.

s_w	τ_1 (s)	τ_2 (s)	c_1	c_2	M_1	M_2	σ_∞ (S/m)	rms (%)
0.75	0.026	1.8872e-07	0.29	0.46	0.042	0.14906	0.081	0.45
0.65	0.038	1.8277e-06	0.58	0.47	0.030	0.11631	0.067	1.1
0.57	0.043	2.6513e-06	0.35	0.56	0.043	0.11824	0.064	0.49
0.52	0.027	1.0785e-06	0.50	0.49	0.027	0.14291	0.051	0.54
0.48	0.034	1.0413e-06	0.49	0.47	0.030	0.12549	0.047	0.47
0.46	0.022	1.0158e-06	0.47	0.51	0.033	0.16574	0.044	0.34
0.40	0.025	1.3898e-06	0.51	0.59	0.035	0.17091	0.029	0.99
0.38	0.030	1.6882e-06	0.44	0.55	0.041	0.19807	0.026	0.48
0.36	0.029	1.0971e-06	0.42	0.56	0.039	0.23866	0.024	0.45
0.35	0.031	1.0093e-06	0.43	0.57	0.041	0.28192	0.022	0.44
0.34	0.038	6.8433e-07	0.45	0.56	0.038	0.34370	0.020	0.70
0.32	0.043	1.1048e-06	0.44	0.56	0.040	0.32041	0.015	0.78
0.31	0.050	6.4349e-07	0.48	0.54	0.036	0.40424	0.015	1.1
0.30	0.035	9.9181e-07	0.41	0.60	0.052	0.35115	0.014	0.60
0.30	0.064	8.0818e-07	0.49	0.54	0.038	0.44896	0.010	1.0
0.28	0.043	8.7294e-07	0.44	0.59	0.049	0.47544	0.0087	0.66

In Figure 11, we plot the two relaxation times as a function of the pore water saturation. The low-frequency relaxation time is fairly constant above the water saturation of 0.20. Its value is around 0.035 s (Figure 11a). It does not display the expected trend with the saturation $\tau_1(s_w) \sim s_w^2$ and therefore would be more related to the grain sizes rather than the pore sizes. Below the critical saturation of 0.20, the increase in the relaxation time could be associated with the formation of microcracks filled with air that would play the role of macroscopic heterogeneities. In Figure 11b, the relaxation time $\tau_2 \approx (8 \pm 4) \times 10^{-6}$ s is independent of the saturation. This may indicate either a control by the clay minerals or a Maxwell-Wagner polarization process as mentioned previously.

Formation factor porosity relationship

The formation factor depends on the porosity according to Archie's law (Archie, 1942) $F = \phi^{-m}$ where m is called the porosity exponent. Figure 12 shows the trends obtained using the data from the present study and other data from the literature. According to Figure 12, m is comprised between 2 and 3 for the COx clay rock, which is consistent with the findings from Jougnot et al. (2009). It follows that the approximation $m \approx n \approx 2.6 \pm 0.4$ is probably a good approximation for the COx clay rock for water saturation above the irreducible water saturation of 0.36.

Influence of the CEC

Figure 13 shows the surface conductivity of various rocks and soils plotted as a function of the CEC divided by the tortuosity (product of the formation factor by the connected porosity). The data for the COx formation fall exactly on the trend obtained with the data set.

Figure 14 shows the relationship between normalized chargeability and surface conductivity for various porous media. If we take the data from Table 1 assuming that the surface conductivity is close to the conductivity of the material at the in situ pore water conductivity, then the COx core sample falls on the trend predicted by the theory (note our procedure implies that the surface conductivity is likely a bit overestimated, which explains why the data fall on the right side of the trend).

Figure 15 shows that the dependence of the surface conductivity with the CEC for the COx is consistent with other data sets for a broad variety of natural porous materials. Similarly, Figure 16 shows that the dependence of the quadrature conductivity with the CEC for the COx is consistent with other data sets. These trends

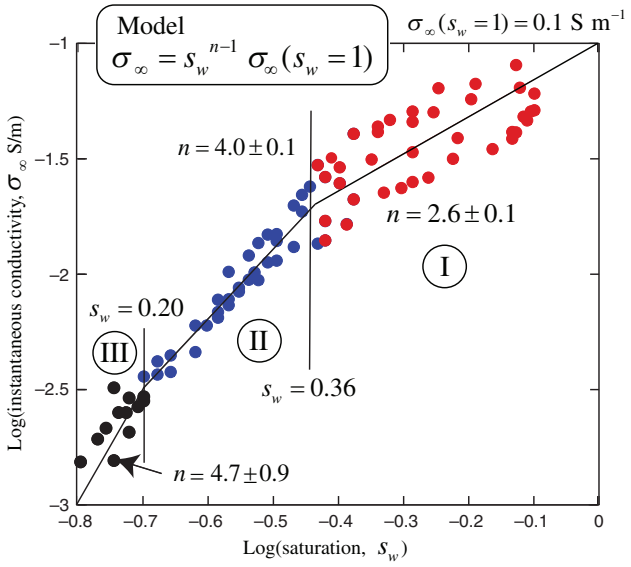

Figure 8. Total instantaneous conductivity versus saturation. The data are fitted with an Archie's type model according to the theory derived in the main text. We observe two values of the saturation exponent depending on if the saturation is above or below a threshold of 0.36, which is considered the irreducible saturation. The domains I, II, and III correspond to the different types of water present in the material. To remove the water in domain III, heating is required, which generates microcracks in the core samples. The saturation value of 0.36 is considered to be the irreducible water saturation.

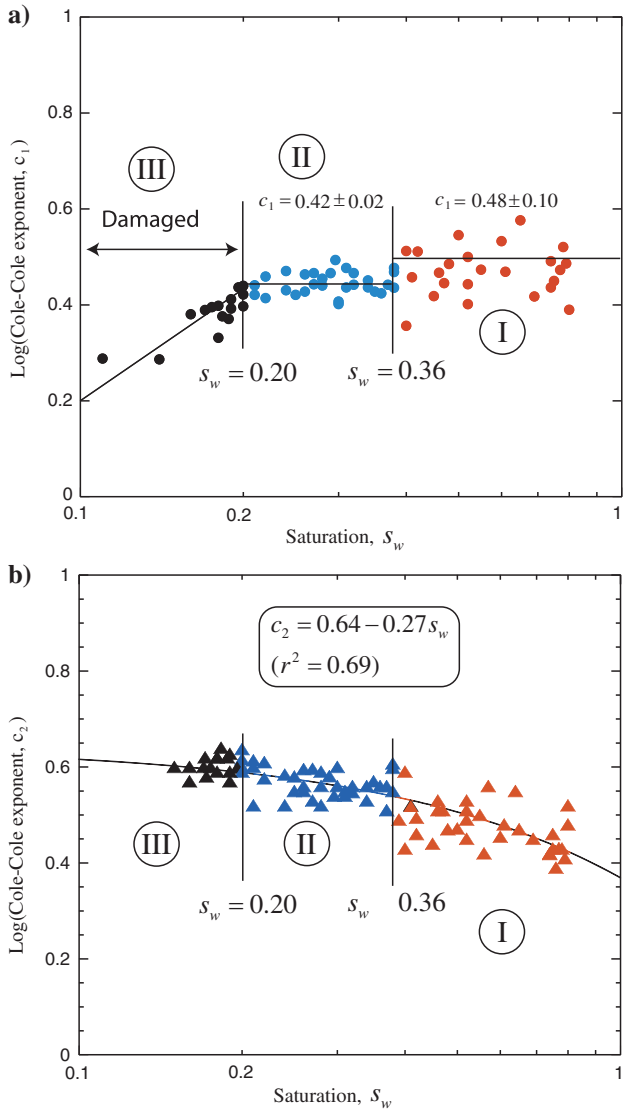

Figure 9. Cole-Cole exponents versus saturation. (a) Low-frequency Cole-Cole exponent c_1. (b) High-frequency Cole-Cole exponent c_2 characterizing the increase of the heterogeneities with the decrease of the water saturation.

confirm that the COx clay rock is characterized by a very high surface conductivity and polarization with respect to other rocks because of its high CEC.

Relative permeability curve

The relative permeability curve is built thanks to the data from Homand et al. (2004), Pham (2006), and Jougnot et al. (2010b) (see Figure 17). This data set is fitted with equation 24. The fitted value of the saturation exponent n = 2.5 is consistent with the value obtained from the complex conductivity measurements

Table 7. Properties of the core samples at saturation (s_w = 1, T = 25°C, and saturated under vacuum with brines).

Sample	σ_∞ (S/m)	M_n (S/m)	F	σ_S (S/m)
EST27906	0.083	0.00498	44.6	0.0498
EST28144	0.062	0.00217	80.7	0.0217
EST29296	0.060	0.00180	80.0	0.0180
EST29300	0.053	0.00302	42.6	0.0302
EST30749	0.123	0.00517	38.0	0.0516
EST59676	0.095	0.00171	33.4	0.0171
EST59674	0.100	0.00260	19.1	0.0260
EST59620	0.138	0.00201	26.2	0.0201

The formation factor F and the surface conductivity σ_S are determined at 1 Hz using the in-phase conductivity (see the procedure in Jougnot et al., 2010a).

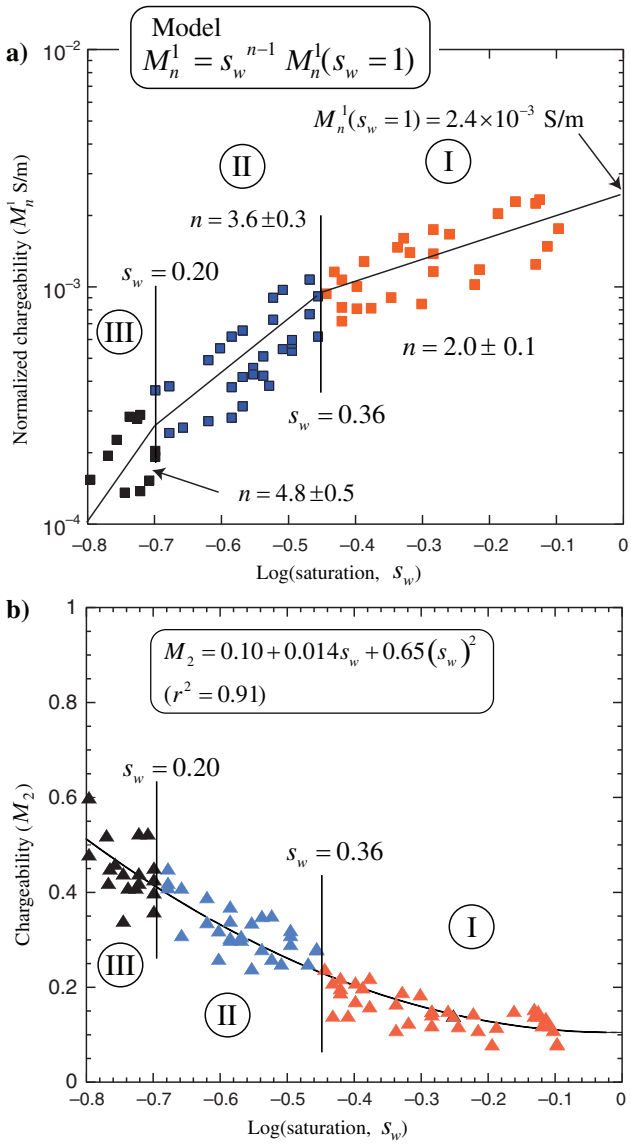

Figure 10. Low- and high-frequency chargeability effects. (a) Low-frequency normalized chargeability versus saturation. (b) High-frequency chargeability versus saturation. This high-frequency chargeability is related to the Maxwell-Wagner polarization. The presence of air in the pore space increases the surface area of contact between different phases of distinct electrical properties increasing the Maxwell-Wagner polarization when the saturation decreases.

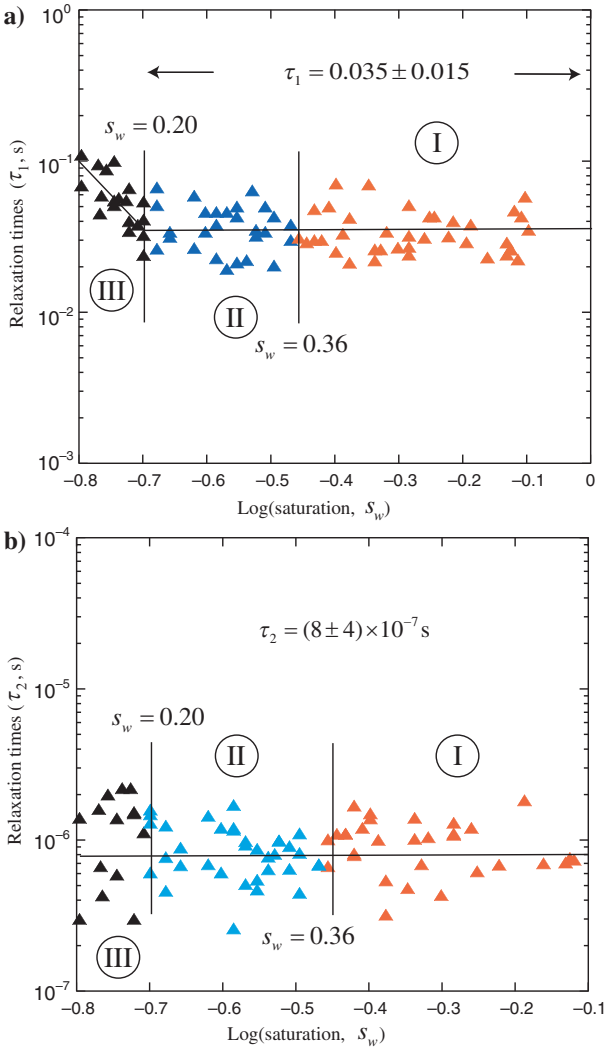

Figure 11. Relation times versus saturation. (a) Low-frequency relaxation time. The increase of the low-frequency relaxation times below the saturation 0.20 is likely related to the formation of microcracks because of the heating process used to reach this low saturation level. (b) High-frequency relaxation time associated with the Maxwell-Wagner polarization. This relaxation time seems independent of the saturation of the water phase.

($n = 2.5 \pm 0.1$). Similarly, the fitted value of the irreducible water saturation $s_w^i = 0.30$ is consistent with the value obtained from the complex conductivity measurements ($s_w^i = 0.36$).

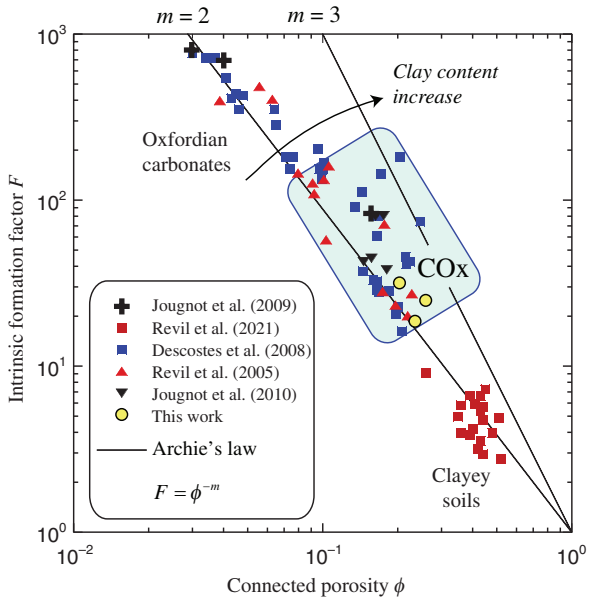

Figure 12. Archie's law for the COx formation. We use the data obtained in the present work (Table 7) and the data from Revil et al. (2005), Descostes et al. (2008), and Jougnot et al. (2009, 2010a, 2010b) including data from the Oxfordian formation located above the COx formation. In addition, we use the data from Revil et al. (2021) for clayey (smectite-rich) soils from the Netherlands.

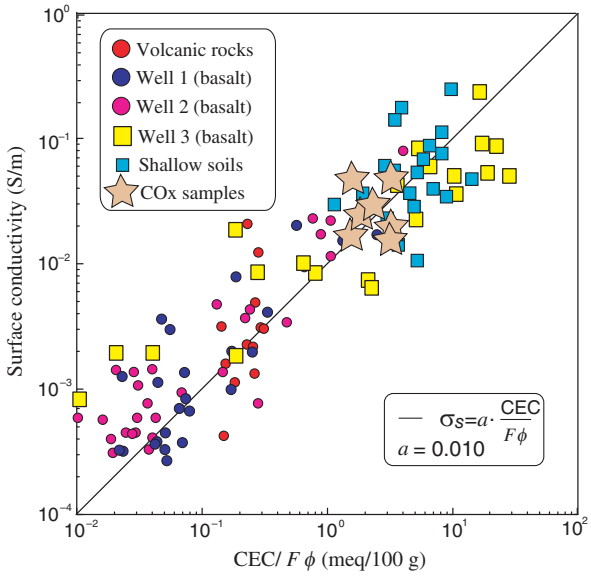

Figure 13. We use the surface conductivities from Table 1 with the formation factor determined from Archie's law with $m = 2.5$ and the surface conductivity data determined from the measured normalized chargeabilities.

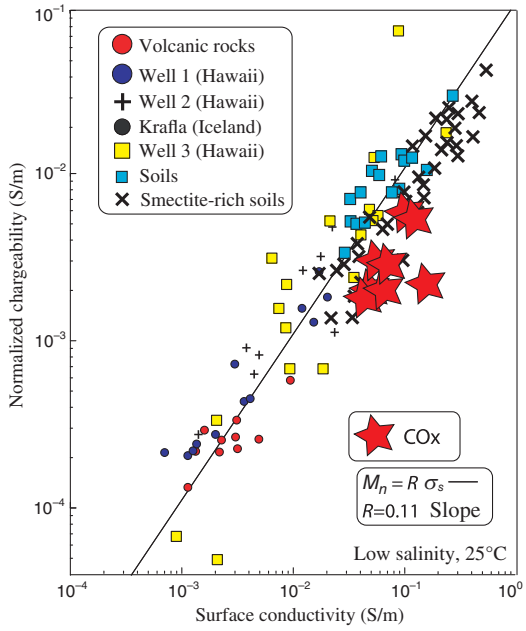

Figure 14. Quadrature conductivity versus surface conductivity. For the COx core samples, we assume that the conductivity is equal to the surface conductivity (data from Table 1), which implies that the surface conductivity is likely overestimated. Soil samples: Revil et al. (2021). Wells 1, 2, and 3 are volcanic rocks from the Kilauea volcano (Hawaii).

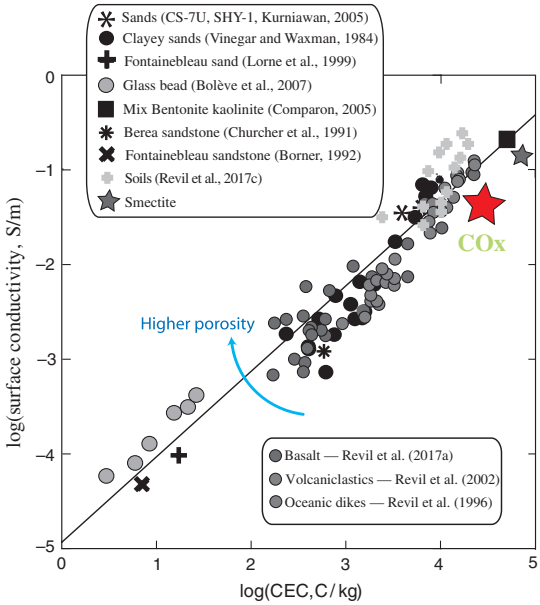

Figure 15. Surface conductivity versus CEC for high-porosity core samples. The data from the literature are from Bolève et al. (2007, glass beads, NaCl), Vinegar and Waxman (1984, shaly sands, NaCl), Churcher et al. (1991, CEC for the Berea sandstone), Lorne et al. (1999, Fontainebleau sand KCl), Kurniawan (2005, clean sand, sample CS-7U), Börner (1992, sample F3 Fontainebleau sandstone), and Comparon (2005, mixtures of MX80 bentonite and kaolinite). The volcanic rock data are from Revil et al. (1996, 2002). The overall trend confirms the linear dependence ($r^2 = 0.94$ in a log-log space) between the surface conductivity and the CEC for the high-porosity core samples.

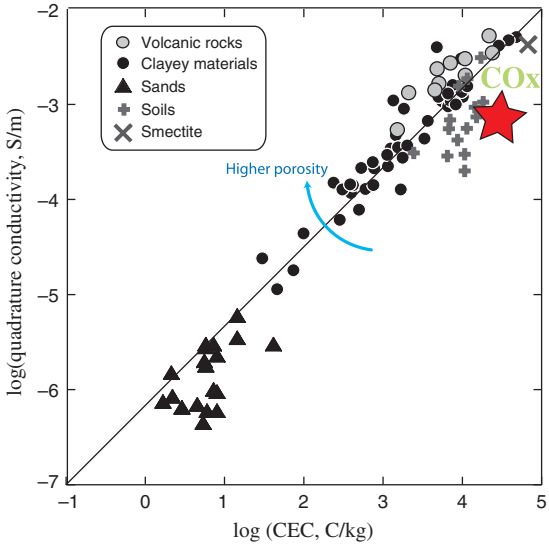

Figure 16. Quadrature conductivity versus CEC for high-porosity core samples. The data shown in the figure are those discussed in Revil et al. (2021). Note: 1 meq/100 g = 963.2 C kg^{-1}. For porous soils and rocks, at full water saturation, the quadrature conductivity (close to 1 Hz) is mostly controlled by the CEC of the material. The overall trend confirms the linear dependence ($r^2 = 0.91$ in a log-log space) between the quadrature conductivity and the CEC for the high-porosity core samples.

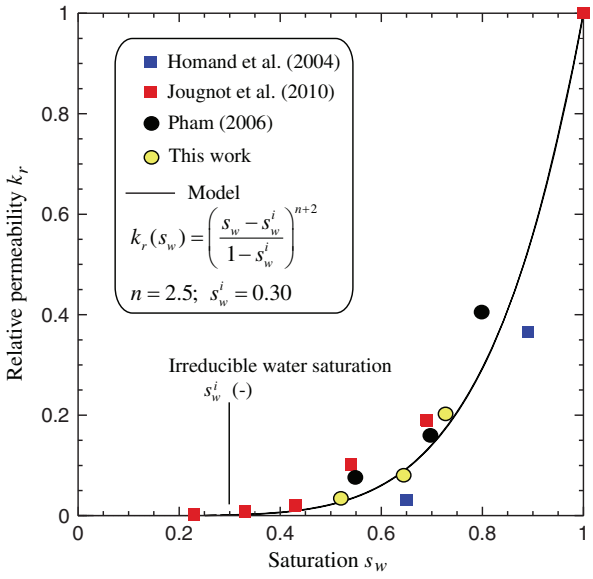

Figure 17. Relative permeability curve. We use three data sets to construct a mean relative permeability curve for the COx formation. The data set is fitted by a power-law function, which requires only the value of the irreducible water saturation and the value of the second Archie's exponent n. For the samples used in the present study, we determine the relative permeability using the approach described in Jougnot et al. (2010b).

CONCLUSION

We investigated the complex conductivity of eight core samples from the COx formation of the Paris Basin in France at different saturations in the range of 0.20–0.80. The complex conductivity spectra were obtained in the frequency range of 1 mHz to 45 kHz. All the data can be fitted by a double Cole-Cole parametric model. The Cole-Cole parameters are investigated as a function of the (water) saturation. The instantaneous conductivity and the normalized chargeability display Archie's type behavior with a saturation exponent $n = 2.6 \pm 0.1$ in the saturation range of 1.0 down to 0.36 and $n = 4.0 \pm 0.1$ in the saturation range of 0.36–0.20. Below a water saturation of 0.20, heating is required to decrease further saturation. The heating process is generating microcracks. The saturation exponent reaches $n = 4.7 \pm 0.1$. The irreducible water saturation is close to 0.36, which is confirmed by the relative permeability curve for the COx core samples. The low-frequency Cole-Cole exponent (close to 0.45 ± 0.03) is essentially independent of the saturation, whereas the high-frequency Cole-Cole exponent decreases slightly with saturation from 0.6 to 0.4. The low- and high-frequency relaxation times are essentially independent of saturation. The low-frequency relaxation time is 0.035 ± 0.015 s above a water saturation of 0.20, whereas the high-frequency relaxation time is $(8 \pm 4) \times 10^{-7}$ s.

The results obtained in this work can be applied to the permeability monitoring of the EDZ. For that purpose, we need to instrument short boreholes and the surface of the galleries to acquire time-lapse complex conductivity data and use the petrophysical model developed in this paper to obtain the water content and the CEC and then to obtain the permeability. In the companion paper, we discuss the effect of anisotropy on the complex conductivity of the COx formation.

ACKNOWLEDGMENTS

We thank E. Zimmermann for his impedance meter. We thank the French National Radioactive Waste Management Agency (ANDRA) for its financial support and for providing the core samples used in this study. A. Revil thanks the French National Research Agency (ANR) through the HYDROGEODAM project under grant no. ANR-17-CE06-0016 for funding his contribution. We thank the editor J. Blanch, V. Lapenna, and an anonymous reviewer for their fruitful comments on our manuscripts.

DATA AND MATERIALS AVAILABILITY

Data associated with this research are available and can be obtained by contacting the corresponding author.

APPENDIX A

POLARIZATION OF THE WATER MOLECULES

The expression for the effective complex pore water conductivity is (Grosse, 2002)

$$\hat{\sigma}_w^* = \sigma_w + i\omega\varepsilon_w^*, \tag{A-1}$$

where σ_w describes the conductivity of the pore water associated with the electromigration of the charge carriers. The dielectric constant ε_w* is complex because of the polarization of the water molecules at very high frequencies. This polarization can be written as

$$\varepsilon_w^* = \varepsilon_w^\infty + \frac{\varepsilon_w - \varepsilon_w^\infty}{1 + i\omega\tau_w}, \tag{A-2}$$

where ε_w denotes the low-frequency ($\omega \ll 2\pi/\tau_w$) permittivity of water ($78.4\varepsilon^0$ at 298.15 K) also called the static permittivity of

water, ε_w^∞ is its high-frequency ($\omega \gg 2\pi/\tau_w$) limit ($5.0\varepsilon^0$ at 298.15 K), ε^0 is the dielectric constant of vacuum ($8.85418781\ldots \times 10^{-12}$ F·m^{-1}), and τ_w is the relaxation time (8.27×10^{-12} s at 298.15 K) associated with the dipolar orientation of the water molecules in an alternating electrical field. It is therefore clear that this polarization process can be neglected with respect to the frequency band investigated in the present paper (less than 45 kHz).

APPENDIX B

INVERSION OF THE COLE-COLE PARAMETERS

The complex conductivity data are fitted with the double Cole-Cole relationship

$$\sigma^* = \sigma_\infty \left(1 - \frac{M_1}{1 + (i\omega\tau_1)^{c_1}} - \frac{M_2}{1 + (i\omega\tau_2)^{c_2}} \right), \qquad \text{(B-1)}$$

where M_1 and M_2 (dimensionless) denote the chargeabilities, c_1 and c_2 (dimensionless) are the two Cole-Cole exponents, and τ_1 and τ_2 are the (relaxation) time constants (s). Indices 1 and 2 refer to lower and higher frequency dispersions, respectively. The high-frequency polarization corresponds to the sum of the clay polarization and Maxwell-Wagner polarization. The low-frequency polarization corresponds to the sum of the large grains and pyrite contributions. With the decrease of the saturation, the pore water conductivity increases so the relaxation time associated with pyrite must decrease (e.g. Martin et al., 2021). Because this effect is not observed in the data, the pyrite polarization can be safely neglected except perhaps at the lowest saturations. Note that the phase for the COx core samples is typically in the range of 10–100 mrad (see Jougnot et al., 2010a, their Figure 13).

The complex conductivity spectra are inverted using a Markov chain Monte Carlo sampling algorithm and a Bayesian approach (Mosegaard and Tarantola, 1995). The model vector of unknown parameters is $\mathbf{m} = [\log(\sigma_0); M_1; c_1; \log(\tau_1); M_2; c_2; \log(\tau_2)]$. Then, the algorithm combines this information with the observed data vector and with the information provided by the double Cole-Cole model to obtain optimal realizations of the model vectors. The root-mean-square (rms) error is given as

$$\mathrm{rms}^2 = \frac{1}{M} \sum_{i=1}^{M} \left(\frac{g^i(\mathbf{m}) - d^i_{\mathrm{obs}}}{d^i_{\mathrm{obs}}} \right)^2, \qquad \text{(B-2)}$$

where M denotes the number of data used in the fitting process and $\mathbf{m}$ is the model vector obtained once the inversion has converged.

REFERENCES

Archie, G. E., 1942, The electrical resistivity log as an aid in determining some reservoir characteristics: Transactions of the AIME, **146**, 54–62, doi: 10.2118/942054-G.

Armand, G., F. Leveau, C. Nussbaum, R. de La Vaissiere, A. Noiret, D. Jaeggi, P. Landrein, and C. Righini, 2014, Geometry and properties of the excavation-induced fractures at the Meuse/Haute-Marne URL drifts: Rock Mechanics and Rock Engineering, **47**, 21–41, doi: 10.1007/s00603-012-0339-6.

Binley, A., L. D. Slater, M. Fukes, and G. Cassiani, 2005, Relationship between spectral induced polarization and hydraulic properties of saturated and unsaturated sandstone: Water Resources Research, **41**, W12417, doi: 10.1029/2005WR004202.

Bleil, D. F., 1948, Induced polarization: A method of geophysical prospecting: Ph.D. thesis, Michigan State College — Department of Physics and Astronomy, 132.

Bleil, D. F., 1953, Induced polarization: A method of geophysical prospecting: Geophysics, **18**, 636–661, doi: 10.1190/1.1437917.

Bolève, A., A. Crespy, F. Revil, F. Janod, and J. L. Mattiuzzo, 2007, Streaming potentials of granular media: Influence of the Dukhin and Reynolds numbers: Journal of Geophysics Research, **112**, B08204, doi: 10.1029/2006JB004673.

Börner, F. D., 1992, Complex conductivity measurements of reservoir properties: Proceedings of the Third European Core Analysis Symposium, Proceedings of the Third European Core Analysis Symposium, Paris, 359–386.

Churcher, R. L., P. R. French, J. C. Shaw, and L. L. Schramm, 1991, International Symposium on Oilfield Chemistry, Paper SPE 21041, Anaheim, 20–22 February.

Cole, K. S., and R. H. Cole, 1941, Dispersion and absorption in dielectrics: Journal of Chemical Physics, **9**, 341–351, doi: 10.1063/1.1750906.

Comparon, L., 2005, Etude expérimentale des propriétés électriques et diélectriques des matériaux argileux consolidés: Ph.D. thesis, Institut de Physique du Globe de Paris, 44 pp., https://hal.archives-ouvertes.fr/tel-00135855.

Cosenza, P., A. Ghorbani, N. Florsch, and A. Revil, 2007, Effects of drying on the low-frequency electrical properties of Tournemire argillites: Pure and Applied Geophysics, **164**, 2043–2066, doi: 10.1007/s00024-007-0253-0.

Cosenza, P., A. Ghorbani, A. Revil, M. Zamora, M. Schmutz, D. Jougnot, and N. Florsch, 2008, A physical model of the low-frequency electrical polarization of clay-rocks: Journal of Geophysical Research, **113**, B08204, doi: 10.1029/2007JB005539.

Descostes, M., V. Blin, F. Bazer-Bachi, P. Meier, B. Grenut, J. Radwan, and E. Tevissen, 2008, Diffusion of anionic species in Callovo-Oxfordian argillites and Oxfordian limestones (Meuse/Haute-Marne, France): Applied Geochemistry, **23**, 655–677, doi: 10.1016/j.apgeochem.2007.11.003.

Dias, C. A., 1972, Analytical model for a polarizable medium at radio and lower frequencies: Journal of Geophysical Research, **77**, 4945–4956, doi: 10.1029/JB077i026p04945.

Dias, C. A., 2000, Developments in a model to describe low frequency electrical polarization of rocks: Geophysics, **65**, 437–451, doi: 10.1190/1.1444738.

Flekkøy, E., 2013, A physical origin of the Cole-Cole description of electrical conductivity: Geophysics, **78**, no. 5, D355–D368, doi: 10.1190/geo2012-0478.1.

Ghorbani, A., P. Cosenza, A. Revil, M. Zamora, M. Schmutz, N. Florsch, and D. Jougnot, 2009, Non-invasive monitoring of water content and textural changes in clay-rocks using spectral induced polarization: A laboratory investigation: Applied Clay Science, **43**, 493–502.

Ghorbani, A., A. Revil, A. Coperey, A. Soueid Ahmed, S. Roque, M. J. Heap, H. Grandis, and F. Viveiros, 2018, Complex conductivity of volcanic rocks and the geophysical mapping of alteration in volcanoes: Journal of Volcanology and Geothermal Research, **357**, 106–127, doi: 10.1016/j.jvolgeores.2018.04.014.

Grosse, C., 2002, Relaxation mechanisms of homogeneous particles and cells suspended in aqueous electrolyte solutions: Interfacial Electrokinetics and Electrophoresis, Surfactant Science Series, **106**, 279–327.

Homand, F., A. Giraud, S. Escoffier, A. Koriche, and D. Hoxha, 2004, Permeability determination of a deep argillite in saturated and partially saturated conditions: International Journal of Heat and Mass Transfer, **47**, 3517–3531, doi: 10.1016/j.ijheatmasstransfer.2004.02.012.

Jamnik, J., and J. Maier, 2001, Generalized equivalent circuits for mass and charge transport: Chemical capacitance and its implications: Physical Chemistry Chemical Physics, **3**, 1668–1678, doi: 10.1039/b100180i.

Jougnot, D., A. Ghorbani, A. Revil, P. Leroy, and P. Cosenza, 2010a, Spectral induced polarization of partially saturated clay-rocks: A mechanistic approach: Geophysical Journal International, **180**, 210–224, doi: 10.1111/j.1365-246X.2009.04426.x.

Jougnot, D., A. Revil, and P. Leroy, 2009, Diffusion of ionic tracers in the Callovo-Oxfordian clay-rock using the Donnan equilibrium model and the electrical formation factor: Geochimica Cosmochimica Acta, **73**, 2712–2726, doi: 10.1016/j.gca.2009.01.035.

Jougnot, D., A. Revil, N. Lu, and A. Wayllace, 2010b, Transport properties of the Callovo-Oxfordian clay rock under partially saturated conditions: Water Resources Research, **46**, W08514, doi: 10.1029/2009WR008552.

Kiewer, M., 2000, Geoelektrische Charakterisierung von Tonformationen: M.Sc. thesis, Technical University Berlin.

Kruschwitz, S., 2002, Detection and characterization of the disturbed rock zone in claystone with complex valued geoelectrics: M.Sc. thesis, Technical University Berlin.

Kruschwitz, S., and U. Yaramanci, 2004, Detection and characterization of the disturbed rock zone in claystone with the complex resistivity method: Journal of Applied Geophysics, **57**, 63–79, doi: 10.1016/j.jappgeo.2004.09.003.

Kurniawan, B., 2005, Shaly sand interpretation using CEC-dependent petrophysical parameters, Ph.D. thesis, Louisiana State University, 201 pp., https://digitalcommons.lsu.edu/gradschool_dissertations/2384.

Leroy, P., A. Revil, A. Kemna, P. Cosenza, and A. Ghorbani, 2008, Complex conductivity of water-saturated packs of glass beads: Journal of Colloid and Interface Science, **321**, 103–117, doi: 10.1016/j.jcis.2007.12.031.
Likos, W. J., and N. Lu, 2003, Automated humidity system for measuring total suction characteristics of clay: Geotechnical Testing Journal, **26**, 179–190.
Lorne, B., F. Perrier, and J.-P. Avouac, 1999, Streaming potential measurements. 1. Properties of the electrical double layer from crushed rock samples.: Journal of Geophysical Research, **104**, 857–877, doi: 10.1029/1999JB900156.
Martin, T., A. Weller, and L. Behling, 2021, Desaturation effects of pyrite-sand mixtures on induced polarization signals: Geophysical Journal International, **228**, 275–290, doi: 10.1093/gji/ggab333.
Mosegaard, K., and A. Tarantola, 1995, Monte Carlo sampling of solutions to inverse problems: Journal of Geophysical Research, **100**, 12431–12447, doi: 10.1029/94JB03097.
Okay, G., P. Cosenza, A. Ghorbani, C. Camerlynck, J. Cabrera, N. Florsch, and A. Revil, 2013, Characterization of macroscopic heterogeneities in clay-rocks using induced polarization: Field tests at the experimental underground research laboratory of Tournemire (Aveyron, France): Geophysical Prospecting, **61**, 134–152, doi: 10.1111/j.1365-2478.2012.01054.x.
Pham, Q. T., 2006, Effets de la désaturation et de la resaturation sur l'argilite dans les ouvrages souterrains: Ph.D. thesis, Ecole Polytechnique/X.
Revil, A., 2013, On charge accumulations in heterogeneous porous materials under the influence of an electrical field: Geophysics, **78**, no. 4, D271–D291, doi: 10.1190/geo2012-0503.1.
Revil, A., D. Hermitte, E. Spangenberg, and J. J. Cochémé, 2002, Electrical properties of zeolitized volcaniclastic materials: Journal of Geophysical Research, **107**, 2168, doi: 10.1029/2001JB000599.
Revil, A., P. Leroy, and K. Titov, 2005, Characterization of transport properties of argillaceous sediments: Application to the Callovo-Oxfordian argillite: Journal of Geophysical Research: Solid Earth, **110**, B06202, doi: 10.1029/2004JB003442.
Revil, A., G. Z. Abdel Aal, E.A. Atekwana, D. Mao, and N. Florsch, 2015b, Induced polarization response of porous media with metallic particles — Part 2. Comparison with a broad database of experimental data: Geophysics, **80**, no. 5, D539–D552, doi: 10.1190/geo2014-0578.1.
Revil, A., A. Coperey, M. J. Heap, and L. Carbillet, 2020, A geophysical index to map alteration, permeability, and mechanical properties within volcanoes. Application to the soft volcanic rocks from Whakaari/White Island (New Zealand): Journal of Volcanology and Geothermal Research, **401**, 106945, doi: 10.1016/j.jvolgeores.2020.106945.
Revil, A., A. Coperey, Z. Shao, N. Florsch, I. L. Fabricius, Y. Deng, J.R Delsman, P.S. Pauw, M. Karaoulis, P. G. B. de Louw, E. S. van Baaren, W. Dabekaussen, A. Menkovic, and J. L. Gunnink, 2017c, Complex conductivity of soils: Water Resources Research, **53**, 7121–7147, doi: 10.1002/2017WR020655.
Revil, A., and N. Florsch, 2010, Determination of permeability from spectral induced polarization data in granular media: Geophysical Journal International, **181**, 1480–1498, doi: 10.1111/j.1365-246X.2010.04573.x.
Revil, A., N. Florsch, and C. Camerlynck, 2014, Spectral induced polarization porosimetry: Geophysical Journal International, **198**, 1016–1033, doi: 10.1093/gji/ggu180.
Revil, A., N. Florsch, and D. Mao, 2015a, Induced polarization response of porous media with metallic particles — Part 1: A theory for disseminated semiconductors: Geophysics, **80**, no. 5, D525–D538, doi: 10.1190/geo2014-0577.1.
Revil, A., A. Ghorbani, D. Jougnot, B. Yven, D. Grgic, F. Bretaudeau, and J. Deparis, forthcoming, Induced polarization of clay-rich materials — Part 2: The effect of anisotropy Geophysics, doi: 10.1190/geo2022-0510.1.
Revil, A., K. Koch, and K. Holliger, 2012, Is it the grain size or the characteristic pore size that controls the induced polarization relaxation time of clean sands and sandstones? Water Resources Research, **76**, A31–A36, doi: 10.1029/2011WR011561.
Revil, A., D. Mao, Z. Shao, M.F. Sleevi, and D. Wang, 2017b, Induced polarization response of porous media with metallic particles — Part 6: The case of metals and semi-metals: Geophysics, **82**, no. 2, E97–E110, doi: 10.1190/geo2016-0389.1.
Revil, A., Y. Qi, N. Panwar, M. Gresse, H. Grandis, R. Sharma, Y. Géraud, N. Chibati, and A. Ghorbani, 2022, Induced polarization images alteration in stratovolcanoes: Journal of Volcanology and Geothermal Research, **429**, 107598, doi: 10.1016/j.jvolgeores.2022.107598.
Revil, A., M. Schmutz, F. Abdulsamad, A. Balde, C. Beck, A. Ghorbani, and S. S. Hubbard, 2021, Field-scale estimation of soil properties from spectral induced polarization tomography: Geoderma, **403**, 115380, doi: 10.1016/j.geoderma.2021.115380.
Revil, A., M. F. Sleevi, and D. Mao, 2017a, Induced polarization response of porous media with metallic particles — Part 5. Influence of the background polarization: Geophysics, **82**, no. 2, E77–E96, doi: 10.1190/geo2016-0388.1.
Revil, A., M. Darot, P. A. Pezard, and K. Becker, 1996, Electrical conduction in oceanic dikes, Hole 504B, *in* J. C. Alt, and H. Kinoshita, eds., Proceedings of ODP Science Research, **148**, College Station, TX (ODP), 297–305.
Sen, P. N., C. Straley, W. E. Kenyon, and M. S. Whittingham, 1990, Surface to-volume ratio, charge density, nuclear magnetic relaxation, and permeability in clay-bearing sandstones: Geophysics, **55**, 61–69, doi: 10.1190/1.1442772.
Tartrat, Y. T., A. Revil, F. Abdulsamad, A. Ghorbani, D. Jougnot, A. Coperey, B. Yven, and R. de la Vaissière, 2019, Induced polarization response of porous media with metallic particles — Part 10. Influence of desiccation: Geophysics, **84**, no. 5, E357–E375, doi: 10.1190/geo2019-0048.1.
Vinegar, H. J., and M. H. Waxman, 1984, Induced polarization of shaly sands: Geophysics, **49**, 1267–1287, doi: 10.1190/1.1441755.
Vinsot, A., F. Leveau, A. Bouchet, and A. Arnould, 2014, Oxidation front and oxygen transfer in the fractured zone surrounding the Meuse/Haute-Marne URL drifts in the Callovian–Oxfordian argillaceous rock: Geological Society, London, Special Publications 400, 207–220.
Volckaert, G., X. Sillen, M. Van Geet, F. Bernier, J. C. Mayor, I. Goebel, P. Bluemling, B. Frieg, and K. Su, 2004, Similarities and differences in the behaviour of plastic and indurated clays, *in* P. F. Ruiz, ed., 6th International Conference on the Management and Disposal of Radioactive Waste — Euradwaste, Radioactive Waste Management — Community Policy and Research Initiatives, 955.
Waxman, M. H., and L. J. M. Smits, 1968, Electrical conductivities in oil bearing shaly sands: SPE Journal, **8**, 107–122.
Yaramanci, U., and M. Kiewer, 2000, Geoelectrical characterization of the disturbed rock zone in opalinus clay (Mont Terri, Switzerland): Proceedings of the 6th EEGS-ES Meeting, Expanded Abstracts, EL 14.
Yven, B., S. Sammartino, Y. Geraud, F. Homand, and F. Villieras, 2007, Mineralogy, texture and porosity of Callovo-Oxfordian argillites of the Meuse/Haute-Marne region (eastern Paris Basin): Mémoires de la Société Géologique de France, **178**, 73–90.
Zimmermann, E., J. Berwix, W. Glaas, H. Meier, H. M. Münch, and A. Kemna, 2007, ZEL-SIP04-V02: User manual: Forschungszentrum Julich GmbH.
Zimmermann, E., A. Kemna, J. Berwix, W. Glaas, H. M. Münch, and J. A. Huisman, 2008, A high-accuracy impedance spectrometer for measuring sediments with low polarizability: Measurement Science and Technology, **19**, 105603, doi: 10.1088/0957-0233/19/10/105603.

Biographies and photographs of the authors are not available.